Journal of Materials Chemistry A

ROYAL SOCIETY OF CHEMISTRY

PAPER

View Article Online
View Journal | View Issue

Cite this: J. Mater. Chem. A, 2026, 14, 12754

Sequential surface synthesis of dispersed sub-nanometer iridium on titanium nitride for acidic water oxidation

Wenhao Liu,[ab] Zhenhua Xie,[c] Lihua Zhang,[a] Jingguang G. Chen, *[cd] Fang Lu *[a] and Yugang Zhang *[a]

Received 24th November 2025
Accepted 6th February 2026

DOI: 10.1039/d5ta09528j

rsc.li/materials-a

Maximizing iridium utilization while maintaining high oxygen evolution reaction (OER) performance remains a persistent challenge in acidic water electrolysis. Immobilizing Ir on conductive, acid-stable supports is promising, yet simultaneously achieving sub-nanometer size, high area coverage, and strong electronic coupling is difficult. Here, we report a sequential surface synthesis on titanium nitride (TiN) that yields uniformly distributed sub-nanometer Ir arrays (~0.7 nm). Our method uses ethylenediaminetetraacetic acid (EDTA) as a temporal scaffold: it chemisorbs to TiN to install dense chelating sites, captures Ir^{3+} ions, and confines Ir cluster growth. A subsequent thermal treatment at 500 °C in a reducing atmosphere removes the ligand shell, while preserving ultrasmall particle size and establishing direct Ir–TiN electronic coupling. The optimized catalyst exhibits mixed Ir^0/Ir^{x+} coordination with low charge-transfer resistance (R_{ct} = 19.2 Ω), delivering a mass activity of 342 A g_{Ir}^{-1} at 1.54 V in acidic electrolyte. *In situ* X-ray absorption spectroscopy reveals irreversible surface oxidation as the primary stability-limiting factor. This stepwise strategy provides a general framework for supported catalysts that maximize precious metal utilization *via* sub-nanometer dispersion.

1. Introduction

Electrochemical water splitting facilitates the storage of renewable electricity as hydrogen fuel.[1–4] Under acidic conditions, the hydrogen evolution reaction (HER: $2H^+ + 2e^- \rightarrow H_2$) at the cathode proceeds efficiently with minimal overpotential. In contrast, the oxygen evolution reaction (OER: $2H_2O \rightarrow O_2 + 4H^+ + 4e^-$) at the anode is kinetically sluggish due to its complex four-electron transfer mechanism, making it the efficiency-limiting step in water electrolysis.[1,2] Among OER catalysts, iridium-based materials uniquely combine high activity with high stability in acidic media, where most other materials rapidly corrode.[2–5] However, Ir is among the rarest elements in the Earth's crust, with a global annual production of only ~7 tons. This scarcity requires maximizing the catalytic utility of every Ir atom through precise structural control.[6–11]

In practical proton exchange membrane water electrolyzers (PEMWEs), the anode operates in strongly acidic environments and at high current densities, which amplifies both kinetic and durability demands on the anode catalyst. Recent PEMWE studies therefore focus on reducing Ir loading while maintaining high utilization through nanoscale dispersion and conductive, corrosion-resistant supports.[12] Our work addresses this design direction by enabling near-monolayer, sub-nanometer Ir dispersion on a conductive metal nitride support as a platform for acidic OER evaluation in half-cell measurements. Critically, particle size governs atomic utilization: shrinking into the sub-nanometer regime (~0.7 nm) renders ≈90% of atoms surface-accessible to the electrolyte, *versus* <30% at 3 nm. However, such ultrasmall clusters cannot exist as stable free-standing entities, and they spontaneously aggregate to minimize surface energy. Strong ligands can stabilize sub-nanometer particles in solution, but these stabilized colloids are difficult to separate from solution and deposit onto electrode supports while maintaining dispersion. Even if sub-nanometer clusters could be deposited, they would rapidly migrate and coalesce under harsh OER conditions (low pH and high anodic potential). This necessitates immobilizing Ir on a conductive, acid-stable support that provides anchoring sites to prevent particle migration while facilitating charge transfer. In addition to providing mechanical and chemical stability under harsh OER conditions, the ideal supported catalyst architecture must satisfy three requirements simultaneously: (i) sub-nanometer Ir particle size to maximize surface exposure,[13] (ii) near-monolayer coverage with uniform distribution to fully

[a]Center for Functional Nanomaterials, Energy & Photon Sciences Directorate, Brookhaven National Laboratory, Upton, NY 11973, USA. E-mail: flu@bnl.gov; yuzhang@bnl.gov
[b]Department of Materials Science and Chemical Engineering, Stony Brook University, Stony Brook, New York 11794, USA
[c]Chemistry Division, Brookhaven National Laboratory, Upton, New York 11973, USA
[d]Department of Chemical Engineering, Columbia University, New York, New York 10027, USA. E-mail: jgchen@columbia.edu

exploit the support surface,[14,15] and (iii) intimate Ir–support contact with low-resistance electronic coupling to enable efficient charge transfer.[16–19]

Titanium nitride (TiN) is a promising support due to its metallic conductivity and acid stability arising from oxidation resistance.[20] However, achieving the ideal Ir architecture on TiN remains challenging. The Adams fusion method, commonly used for supported Ir oxides, provides intimate metal–support contact but typically yields particles > 5 nm due to uncontrolled growth at temperatures > 500 °C. Recent colloidal approaches using poly(amidoamine) dendrimers or cetyltrimethylammonium bromide (CTAB) have reduced particle sizes to 2–5 nm IrO_x on TiN,[21] but this still exceeds the sub-nanometer target required for maximum utilization. Moreover, the inertness of TiN often necessitates harsh pre-activation (*e.g.*, hydroxylation) that partially oxidizes the surface, compromising conductivity. Most critically, all current methods face a persistent challenge: strong ligands that enable sub-nanometer particle formation simultaneously prevent high-density surface attachment and create insulating barriers that block charge transfer, while weak or absent ligands allow surface contact but cause aggregation. This paradox arises because conventional one-pot approaches attempt to control particle size and surface anchoring simultaneously, inevitably forcing compromises on both.

Resolving this problem requires a multifunctional additive that (i) activates the support surface, (ii) captures metal ions, and (iii) confines cluster growth, and, crucially, deploys these functions sequentially to decouple competing processes. Ethylenediaminetetraacetic acid (EDTA), a hexadentate chelating agent, is well suited for these roles. First, EDTA can chemisorb to undercoordinated Ti sites on TiN, installing a high density of anchoring motifs across the support. Second, these surface-bound chelating groups remain available to capture Ir^{3+} from solution. Third, EDTA's cage-like coordination provides steric barriers that restrict particle coalescence, enabling sub-nanometer cluster formation. When these three functions operate simultaneously in conventional one-pot synthesis, stable Ir–EDTA complexes form in solution and resist surface deposition, resulting in poor coverage and ligand-blocked interfaces. However, exploiting these functionalities in a deliberate sequence can circumvent the size-*versus*-attachment limitation.

Here, we demonstrate a sequential surface synthesis strategy that decouples these competing requirements through four stages: (i) pre-functionalize TiN with EDTA to create high-density chelation sites, (ii) capture Ir^{3+} at these pre-installed anchor sites, (iii) reduce *in situ* to form sub-nanometer Ir while maintaining spatial confinement, and (iv) thermally remove organic residues without inducing sintering. This anchor-before-loading, then clean-after-formation workflow enables independent optimization of each step, in contrast to conventional one-pot syntheses where all processes compete simultaneously.

This methodology produces ~0.7 nm Ir arrays with near-monolayer coverage on TiN supports. Thermal activation at 500 °C in a melamine/N_2 atmosphere removes EDTA residues while preserving the sub-nanometer architecture, yielding a catalyst with coexisting Ir–O and Ir–Ir bonds. The resulting Ir@TiN-500 catalyst exhibits a mass activity of 342 A g_{Ir}^{-1} at 1.54 V *vs.* RHE, outperforming commercial IrO_2. *In situ* X-ray absorption spectroscopy (XAS) results reveal potential-induced Ir oxidation with limited reversibility, explaining the observed stability limitation. This work establishes sequential surface synthesis as a methodology for creating well-defined supported metal catalysts, with potential applicability beyond the Ir/TiN system demonstrated here.

2. Experimental section

2.1 Chemicals

Iridium(III) chloride hydrate ($IrCl_3 \cdot xH_2O$, 99.9%), sodium borohydride ($NaBH_4$, 99.99%), ethylenediaminetetraacetic acid disodium salt dihydrate (EDTA-$Na_2 \cdot 2H_2O$, reagent grade), and melamine were purchased from Sigma-Aldrich. Perchloric acid ($HClO_4$, 69%) was obtained from OmniTrace. Nafion solution (D521, ~10 wt%) was purchased from Ion-Power. All chemicals were used as received. Deionized water (resistivity > 18 MΩ cm) was used throughout.

2.2 Synthesis of the TiN support

Titanium nitride nanoparticles were synthesized following a previously reported method.[22] The as-synthesized TiN (150 mg) was acid-treated by dispersion in 50 mL of 37% HCl, followed by ultrasonication for 10 minutes and heating at 65 °C for 24 hours. The acid-treated TiN was collected by centrifugation, washed with DI water and ethanol, and dried under vacuum at 60 °C overnight.

2.3 Synthesis of the Ir@TiN precursor

The sequential surface synthesis was performed in three steps with intermediate washing. (1) EDTA anchoring: EDTA-$Na_2 \cdot 2H_2O$ (3.72 g, 0.01 mol) was dissolved in 10 mL of 1 M NaOH. Acid-treated TiN (62.5 mg) was dispersed in 12.5 mL of the EDTA solution and stirred at 300 rpm at 80 °C for 24 hours. The EDTA-anchored TiN was collected by centrifugation, washed extensively with DI water, and redispersed for the next step. (2) Ir^{3+} capture: the EDTA-functionalized TiN was added to 50 mL of $IrCl_3$ solution (5 mM in DI water) and stirred at 300 rpm at 80 °C for 24 hours. The Ir^{3+}-loaded TiN was collected by centrifugation and washed thoroughly with DI water. (3) *In situ* reduction: the Ir^{3+}-loaded TiN was redispersed in ethanol, and 12.5 mL of freshly prepared $NaBH_4$ solution (0.1 M in ethanol) was added dropwise under stirring at 300 rpm. The reduction was continued for 24 hours at room temperature. The resulting Ir@TiN precursor was collected by vacuum filtration, washed with DI water and ethanol, and dried under vacuum at 80 °C overnight.

2.4 Synthesis of the Ir@TiN-*T* series

The Ir@TiN precursor was thermally activated by annealing at various temperatures (400, 500, 600, 700, or 800 °C) under a melamine/N_2 atmosphere for 2 hours with a heating ramp of 5

°C min^{-1}. Melamine served as a nitrogen-rich reducing agent to prevent TiN oxidation during organic residue removal. The resulting materials are denoted as Ir@TiN-*T*, where *T* represents the annealing temperature.

2.5 Materials characterization

X-ray diffraction (XRD) patterns were collected using a Rigaku Miniflex II diffractometer with Cu Kα radiation ($\lambda = 1.54$ Å) over the 2θ range of 10–80°. Transmission electron microscopy (TEM) images were acquired on a JEOL JEM-1400 microscope. High-resolution TEM (HRTEM), high-angle annular dark-field scanning TEM (HAADF-STEM), and energy-dispersive X-ray spectroscopy (EDX) elemental mapping were performed using a FEI Talos 200X microscope. X-ray photoelectron spectroscopy (XPS) measurements were conducted using a spectrometer equipped with an Al Kα X-ray source (1486.6 eV). X-ray absorption spectroscopy (XAS) measurements at the Ir L_3-edge were performed at beamline 7-BM (QAS) of the National Synchrotron Light Source II (NSLS-II) at the Brookhaven National Laboratory. Spectra were collected in fluorescence mode using a passivated implanted planar silicon (PIPS) detector. XAS data were processed using the IFEFFIT software package.

2.6 Electrochemical measurements

All electrochemical measurements were performed using a Bio-Logic VMP-3e multichannel potentiostat in O_2-saturated 0.1 M $HClO_4$ electrolyte at room temperature. A standard three-electrode configuration was employed with a rotating glassy carbon electrode (GCE, diameter: 5 mm, and geometric area: 0.196 cm^2) as the working electrode operated at 1600 rpm, Ag/AgCl (saturated KCl) as the reference electrode, and Pt foil as the counter electrode.

Catalyst inks were prepared by dispersing 3.96 mg of catalyst in a mixture of 75 μL ethanol, 25 μL isopropyl alcohol, and 3 μL Nafion D521 solution, followed by ultrasonication. The ink was drop-cast onto the GCE to achieve an Ir mass loading of 20 μg_{Ir} cm^{-2}. Linear sweep voltammetry (LSV) curves were recorded at 20 mV s^{-1} with 85% *iR* compensation after cyclic voltammograms stabilized. All potentials were converted to the reversible hydrogen electrode (RHE) scale using $E(\mathrm{RHE}) = E(\mathrm{Ag/AgCl}) + 0.197\ \mathrm{V} + 0.059 \times \mathrm{pH}$. Electrochemical impedance spectroscopy (EIS) was performed at open-circuit potential over a frequency range of 100 kHz to 0.1 Hz with an AC amplitude of 10 mV. Chronopotentiometry stability tests were conducted at a constant current density of 10 mA cm^{-2} for up to 10 hours.

2.7 *In situ* X-ray absorption spectroscopy

In situ XAS measurements were conducted at beamline 7-BM (QAS) of NSLS-II using a custom three-electrode electrochemical cell with a Kapton window. The working electrode was prepared by drop-casting catalyst ink onto carbon paper. Measurements were collected at the Ir L_3-edge in fluorescence mode while applying controlled potentials from open-circuit voltage to 1.6 V *vs.* RHE in O_2-saturated 0.1 M $HClO_4$. Spectra were recorded after holding each potential for 10 minutes to ensure steady-state conditions.

3. Results

3.1 Design principle of sequential surface synthesis

The synthesis challenge outlined above requires simultaneously achieving sub-nanometer size, high surface coverage, and direct electronic coupling between Ir and TiN. Fig. 1a illustrates why conventional single-step approaches fail to satisfy all three requirements, using three representative cases. (i) No capping ligands: Ir undergoes uncontrolled growth and coalescence, yielding large aggregates themselves, without specific interaction with the support. (ii) Weak ligands: modest size control reduces coalescence, but weak binding interaction with TiN leads to patchy, nonuniform coverage with visible, bare support regions. (iii) Strong chelating ligands (one-pot): hexadentate, cage-like coordination produces the smallest particles in solution, yet the resultant kinetically stable Ir–ligand complexes resist adsorption onto chemically inert TiN, causing material loss to the liquid phase. The few complexes that do deposit retain their protective ligand shells, creating insulating organic barriers between Ir and TiN, blocking charge transfer and preventing direct Ir–TiN coupling. This reveals a persistent limitation: in one-pot synthesis, the same molecular property (strong Ir–ligand coordination) that enables sub-nanometer confinement simultaneously undermines high-density coverage and charge transfer between Ir and TiN. The scoring matrix in Fig. 1a captures this limitation: no conventional single-step method satisfactorily meets more than one of the three criteria.

Our sequential strategy (Fig. 1b) resolves this by temporally separating EDTA functions rather than exploiting them simultaneously. The key insight is spatial pre-organization: by first installing EDTA as a surface-bound template on TiN before introducing the Ir precursor, we reverse the thermodynamic preference from solution-phase complexation to surface-directed coordination. In step 1, acid-treated TiN is functionalized with EDTA in the absence of Ir, allowing the chelating agent to chemisorb to undercoordinated surface Ti sites through its carboxylate groups. After washing to remove unbound EDTA, the support surface is decorated with a high-density array of anchored chelation sites with their metal-binding amine groups oriented outward. In step 2, Ir^{3+} is introduced. Since no excess EDTA remains in solution, Ir^{3+} coordinates exclusively to these immobilized sites rather than forming free solution complexes. This spatial confinement is critical: because each Ir center is pre-anchored to a specific surface location, subsequent reduction becomes a heterogeneous surface-confined process rather than homogeneous solution-phase nucleation. In step 3, addition of $NaBH_4$ reduces Ir^{3+} to metallic Ir^0. The surface-bound EDTA scaffold maintains spatial isolation between adjacent nucleation sites, preventing migration and coalescence during reduction, enabling the formation of sub-nanometer clusters in intimate contact with the underlying TiN support. However, the as-synthesized material retains residual EDTA coordination that electronically isolates Ir from TiN. Step 4 addresses this through controlled thermal treatment in a reducing atmosphere

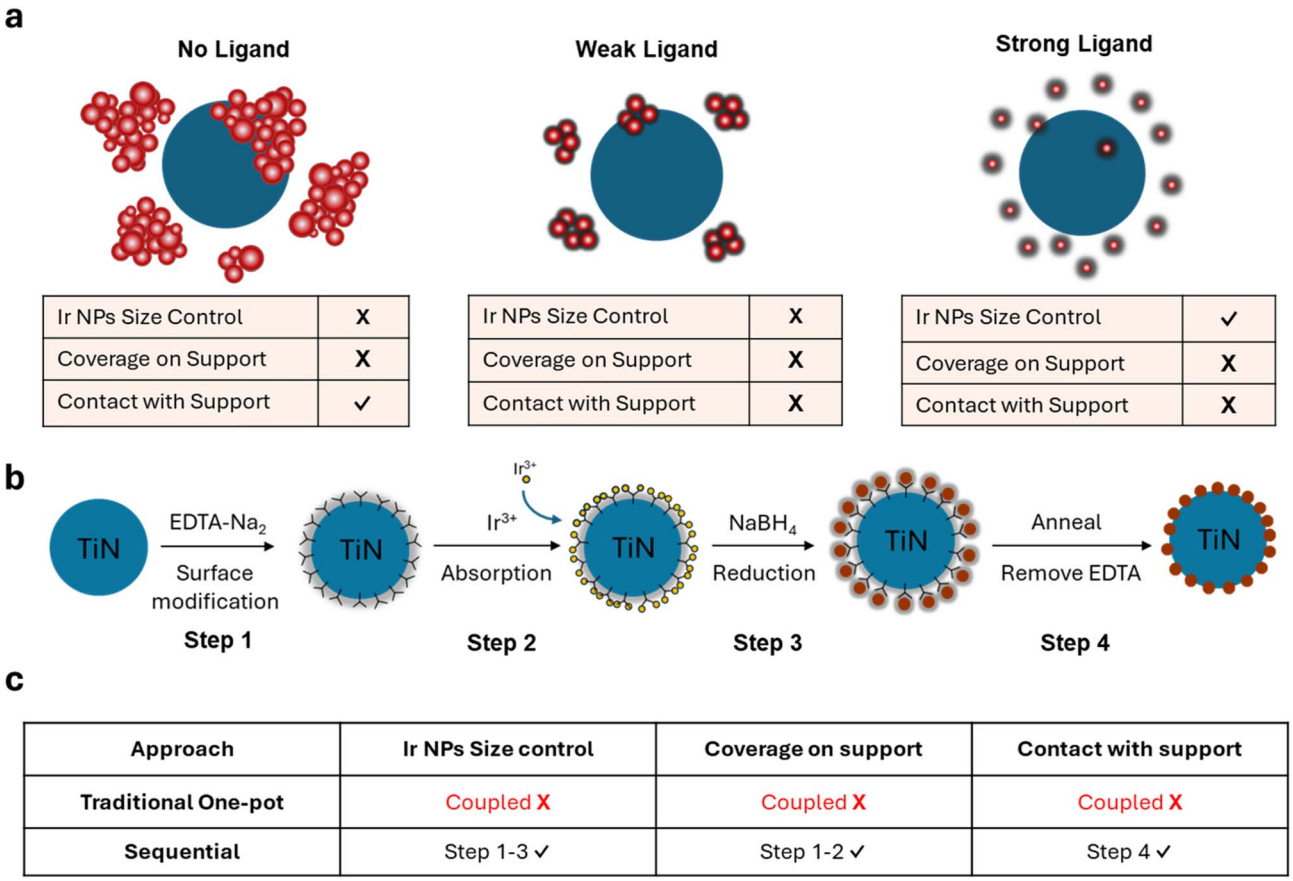

Approach	Ir NPs Size control	Coverage on support	Contact with support
Traditional One-pot	Coupled X	Coupled X	Coupled X
Sequential	Step 1-3 ✓	Step 1-2 ✓	Step 4 ✓

Fig. 1 Sequential surface synthesis design principle. (a) Conventional one-pot approaches and their limitations. Without ligands: large aggregates. Weak ligands: moderate size and poor coverage. Strong ligands: sub-nanometer particles in solution but low surface deposition and electronic blocking. The big blue particle and small red particles correspond to the support and the colloidal catalytic nanoparticles in the solution. The scoring table quantifies performance against three requirements. (b) Sequential synthesis strategy: EDTA pre-anchoring, Ir^{3+} capture, confined reduction, and thermal activation. (c) Comparison table showing independent optimization of each requirement.

(melamine/N_2), thermally decomposing the organic EDTA residues. Critically, the Ir–TiN interaction established during surface-directed reduction (step 3) is sufficiently strong to prevent sintering during organic removal, preserving the sub-nanometer architecture while simultaneously cleaning the interface to enable direct electronic coupling.

This sequential workflow converts an unfavorable process (depositing kinetically stable Ir–EDTA complexes onto inert TiN) into a favorable one (capturing Ir^{3+} at pre-installed, surface-bound chelation sites). Each stage addresses a specific requirement: EDTA anchoring enables high-density coverage (requirement (ii)), surface-confined Ir^{3+} capture followed by reduction achieves sub-nanometer size (requirement (i)), and thermal activation establishes direct contact between Ir and TiN (requirement (iii)). Unlike one-pot synthesis, where all processes compete, the sequential approach allows independent optimization of each step.

3.2 Experimental comparison of synthesis methods

To validate this design principle, we systematically compared four synthesis strategies, including (i) no ligand (direct reduction), (ii) weak ligand (CTAC), (iii) strong ligand co-deposition (conventional one-pot EDTA method), and (iv) strong ligand pre-anchoring (our sequential EDTA method). Fig. 2a–d present transmission electron microscopy (TEM) images of each approach. Without surface capping ligands (Fig. 2a), Ir forms agglomerations of hundreds of nanometers comprising large irregular primary particles. Quantitative particle size distribution analysis from more than 100 particles per sample shows an average size of 3.8 ± 1.3 nm (Fig. 2e), confirming uncontrolled nucleation and coalescence. Coverage analysis reveals that less than ~30% of the TiN surface area is occupied by Ir nanoparticles (Fig. 2f), with extensive bare regions clearly visible.

CTAC-mediated synthesis (Fig. 2b) provides moderate improvement, yielding primary particles with a mean diameter of 1.6 ± 0.3 nm (Fig. 2e). However, these particles form agglomerations of ~100 nm on the TiN surface, achieving only 41% surface coverage (Fig. 2f). The distribution remains heterogeneous with clearly visible uncoated areas. The one-pot EDTA co-deposition approach (Fig. 2c) produces sub-nanometer primary particles with a size of 0.8 ± 0.2 nm, substantially smaller than both the no-ligand and CTAC cases. However, it only achieves ~48% surface coverage (Fig. 2f), which still leaves many bare regions. This confirms the challenge outlined in

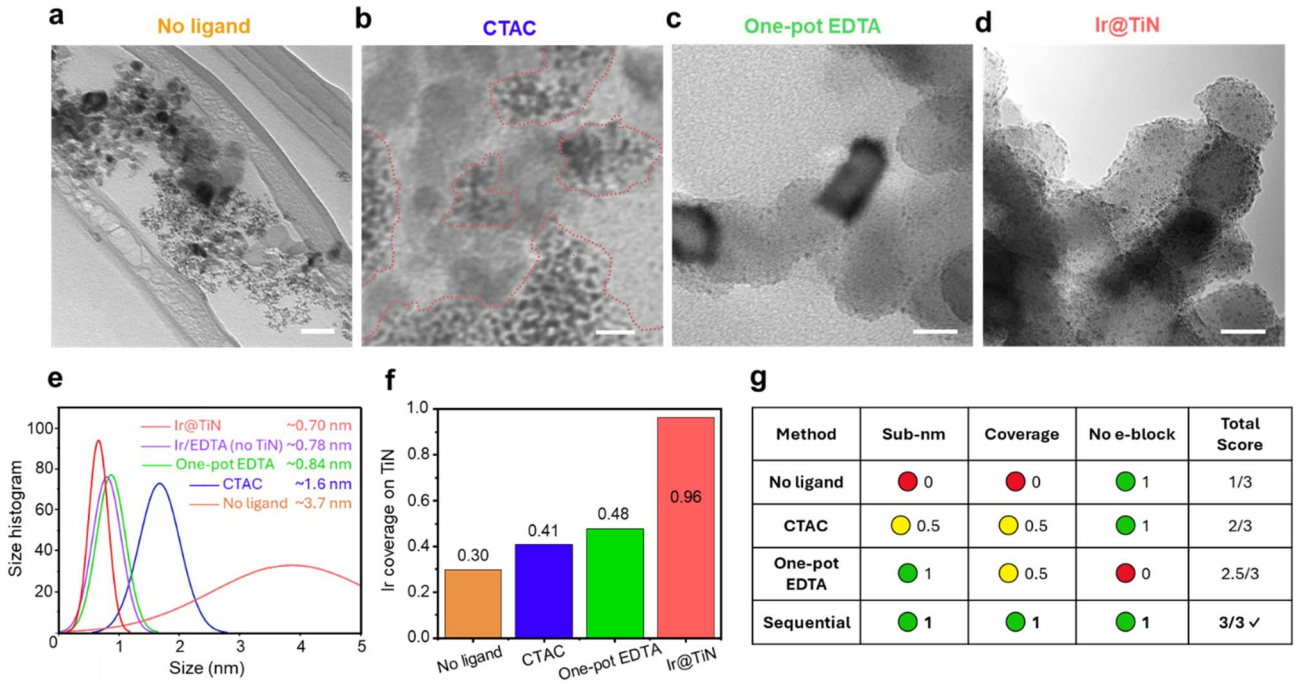

Method	Sub-nm	Coverage	No e-block	Total Score
No ligand	0	0	1	1/3
CTAC	0.5	0.5	1	2/3
One-pot EDTA	1	0.5	0	2.5/3
Sequential	1	1	1	3/3 ✓

Fig. 2 Experimental comparison of synthesis methods. (a–d) TEM images of the four approaches. (a) No ligand: large aggregates, 30% coverage. (b) CTAC: 1.65 ± 0.34 nm particles, 41% coverage. (c) One-pot EDTA: 0.84 ± 0.23 nm but only 48% coverage. (d) Sequential EDTA: 0.70 ± 0.16 nm, up to 96% coverage. (e) Size histograms (the particle size distribution was obtained from TEM images and fitted with a Gaussian curve) from >100 particles. (f) Coverage analysis. (g) Scoring matrix against three requirements. The scale bars in (a–d) are 50, 10, 10, and 10 nm, respectively.

Section 2.1: kinetically stable solution-phase Ir–EDTA complexes that enable size control simultaneously resist adsorption on the TiN surface.

In contrast, the sequential EDTA pre-anchoring approach (Fig. 2d) produces uniform sub-nanometer particles with a mean diameter of 0.70 ± 0.16 nm (Fig. 2e) that densely decorate the TiN surface with ~96% coverage (Fig. 2f), which is more than a tenfold improvement over the no-ligand control and more than a fourfold improvement over one-pot EDTA. No large aggregates or bare regions are observed across multiple imaging areas. The narrow size distribution indicates uniform nucleation kinetics consistent with templated growth at pre-defined surface sites. To clarify the support role of TiN, we prepared a control sample without TiN, in which the Ir precursor was reduced in the presence of EDTA in solution (denoted as Ir/EDTA, no TiN; Fig. 2e and S3). TEM shows that EDTA can temporarily stabilize ultrasmall Ir clusters (~0.78 nm). However, this dispersion remains ligand-capped, which is expected to partially block surface sites and hinder electron transfer to the electrode substrate during electrochemical testing. Attempts to remove EDTA without a solid anchoring surface lead to aggregation, so this TiN-free sample serves as a structural control rather than an electrochemical benchmark for metal–support coupling. This underscores the essential role of TiN anchoring in enabling ligand removal while preserving sub-nanometer dispersion.

The performance scoring matrix (Fig. 2g) quantifies these observations against the three criteria: sub-nanometer size, high coverage, and unobstructed contact. The no-ligand method provides contact but fails on size and coverage. CTAC achieves partial scores on all metrics but excels at none. One-pot EDTA succeeds on size but fails on coverage and electronic contact due to residual ligand shells. Only sequential synthesis satisfies all requirements simultaneously.

3.3 Thermal optimization and structural characterization

Despite achieving the desired sub-nanometer morphology, the as-synthesized Ir@TiN precursor exhibits poor OER activity (33 A g_{Ir}^{-1}) compared with commercial IrO_2 (76 A g_{Ir}^{-1}). This is consistent with residual EDTA coordination electronically isolating Ir clusters from the TiN support. Electrochemical impedance spectroscopy (EIS) confirms this, revealing a high charge-transfer resistance (R_{ct} > 380 Ω).

To address this insulating barrier while preserving the sub-nanometer architecture, we performed a systematic thermal treatment study at 400, 500, 600, 700, and 800 °C under a melamine/N_2 atmosphere. Melamine serves as a nitrogen-rich reducing agent that decomposes at elevated temperatures to generate NH_3 and other reducing species, preventing TiN oxidation while facilitating organic decomposition. This optimization study (detailed in Section 3.4) identifies 500 °C as the optimal condition, achieving EDTA removal without inducing sintering. Fig. 3 presents structural characterization of the optimized Ir@TiN-500 catalyst.

Transmission electron microscopy reveals uniform Ir distribution across multiple length scales (Fig. 3). Low-magnification

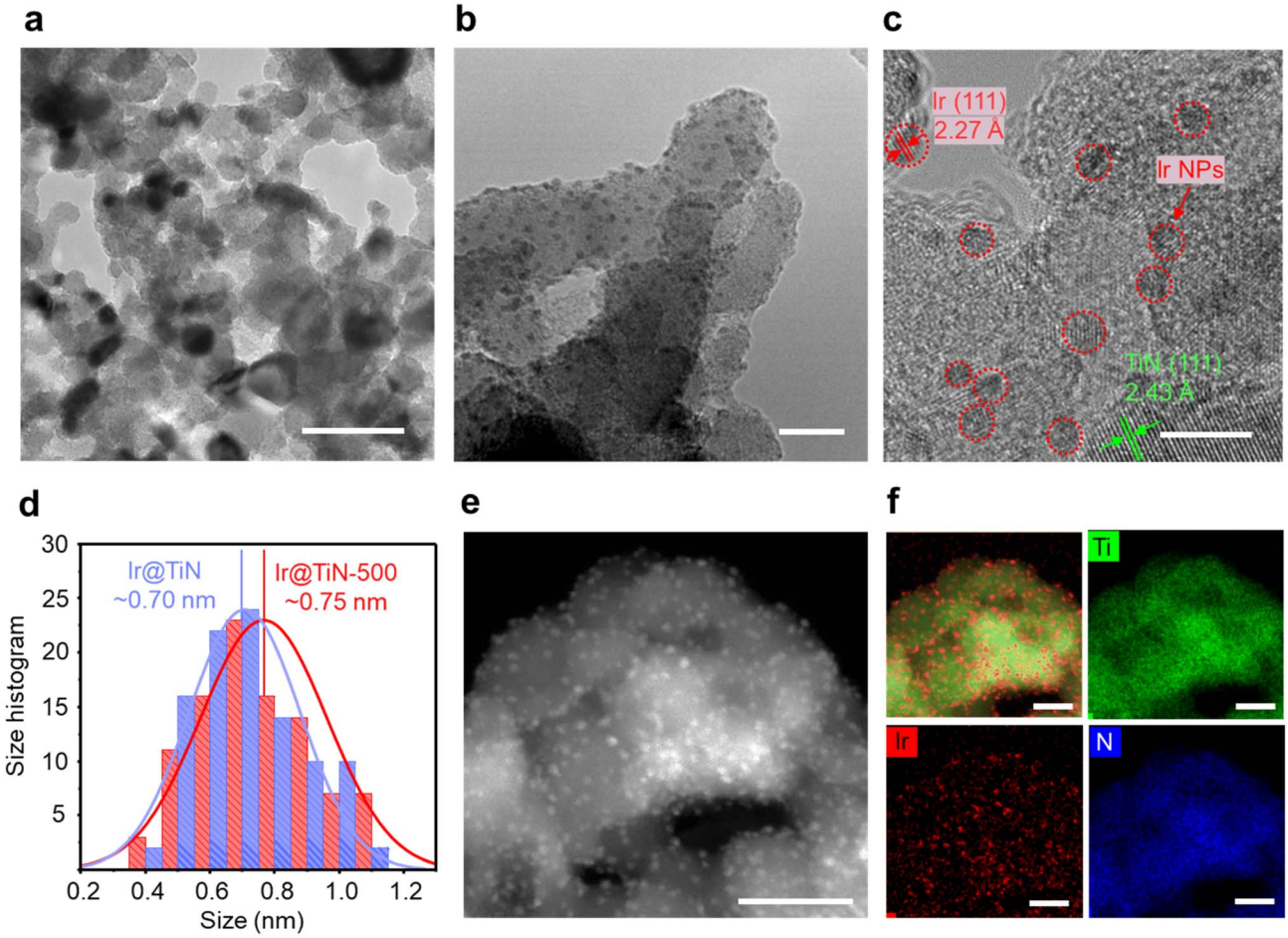

Fig. 3 Structural characterization of Ir@TiN-500. (a) Low-magnification TEM showing uniform Ir decoration. (b) High-magnification TEM showing a dense Ir array, with a mean size of around 0.7 nm (scale bar = 10 nm). (c) HRTEM showing Ir(111) fringes ($d \approx 0.227$ nm) and TiN(111) fringes ($d \approx 0.243$ nm). (d) Size histogram: 0.75 ± 0.20 nm Gaussian distribution. (e) HAADF-STEM image. (f) EDX elemental mapping. The scale bars are 50, 10, and 5 nm in (a–c) and 20 and 10 nm in (e and f), respectively.

TEM (Fig. 3a) shows multiple TiN nanoparticles uniformly decorated with sub-nanometer Ir, with no preferential deposition on specific regions or crystal facets, confirming that high-density coverage extends across the entire sample. Medium-magnification TEM (Fig. 3b) reveals a dense array of discrete Ir nanoparticles covering approximately 90% of the TiN support surface.

High-resolution TEM (Fig. 3c) shows the crystalline nature of individual Ir nanoparticles. Clear lattice fringes with a *d*-spacing of 0.22 nm correspond to the Ir(111) planes of face-centered cubic metallic iridium. Both Ir and TiN lattices are visible with no amorphous structure at the interface, indicating that thermal treatment has eliminated the EDTA coordination shell without triggering sintering. The particle size histogram (Fig. 3d) shows a narrow Gaussian distribution centered at 0.75 ± 0.2 nm.

High-angle annular dark-field scanning TEM (HAADF-STEM, Fig. 3e) shows bright Ir nanoparticles uniformly distributed across the darker TiN support. The particle density is comparable to the as-synthesized sequential material (Section 3.2), further confirming that thermal treatment does not cause particle migration or coalescence. Energy-dispersive X-ray spectroscopy elemental mapping (Fig. 3f) shows spatial overlap of Ir, Ti, and N signals across the mapped region, indicating uniform distribution with no phase segregation or Ir-rich domains. The homogeneous Ir signal across multiple TiN grains demonstrates reproducible coating independent of local variations in support morphology.

3.4 Temperature-dependent structural and electronic evolution

To understand why 500 °C is optimal, we systematically characterized the thermal series from 400 to 800 °C using TEM, X-ray diffraction (XRD), X-ray photoelectron spectroscopy (XPS), and X-ray absorption spectroscopy (XAS). This multi-modal characterization reveals a narrow temperature window where EDTA removal and sub-nanometer size retention coincide.

3.4.1 Morphological and structural properties. TEM reveals distinct outcomes at different temperatures (Fig. 4a). At 400 °C and 500 °C, Ir particles remain in the sub-nanometer regime (0.7–0.8 nm), indicating that thermal treatment up to 500 °C

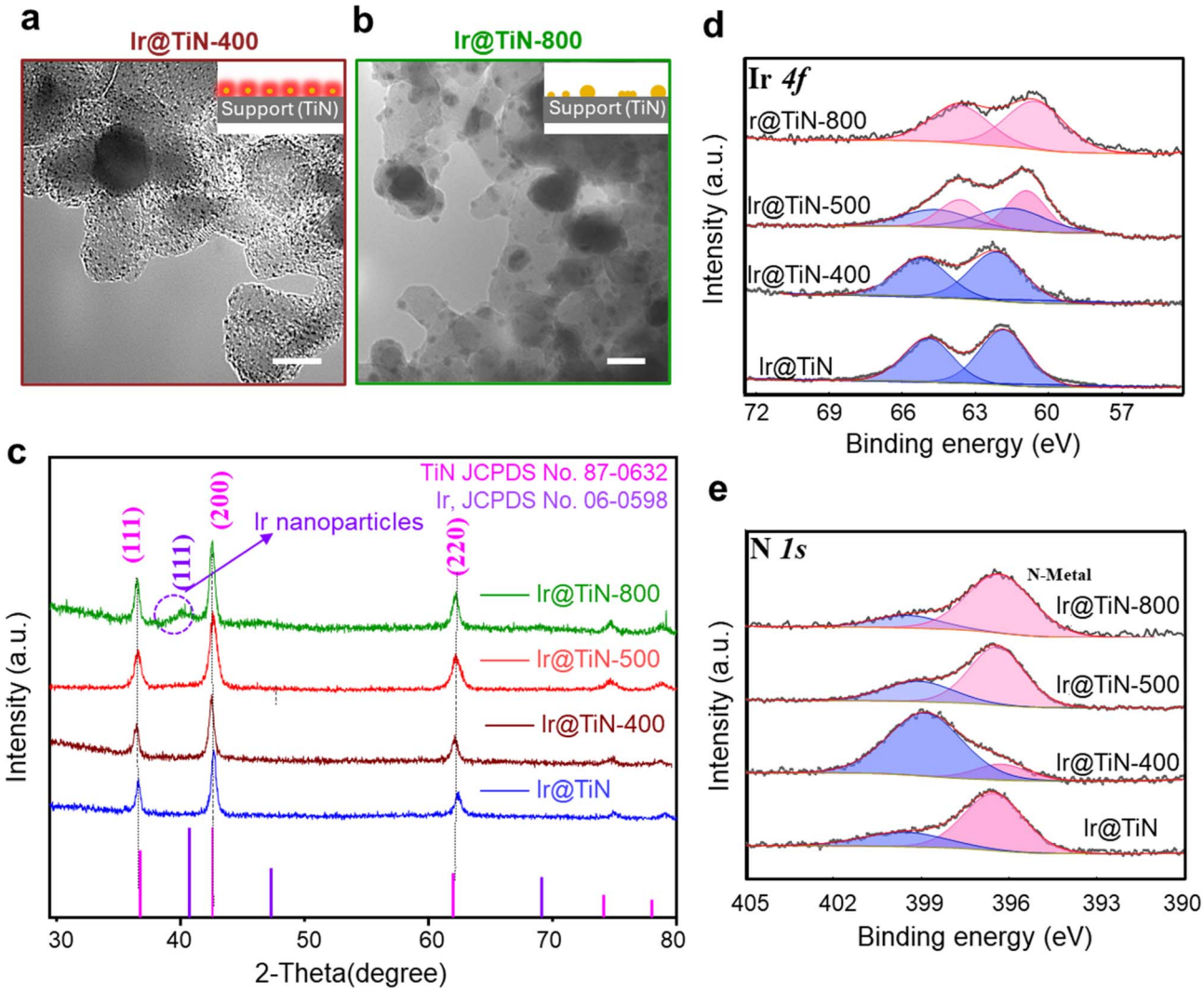

Fig. 4 Temperature-dependent structural and chemical properties. (a and b) TEM at different temperatures: (a) 400 °C maintains 0.7 nm particles; (b) 800 °C shows sintering to 1–5 nm. Scale bars = 5 nm. (c) XRD patterns showing a stable TiN phase; Ir peaks appear only at 800 °C. (d) XPS Ir 4f spectra: 400 °C predominantly oxidized, 500 °C mixed Ir^0/Ir^{x+}, and 800 °C fully metallic. (e) XPS N 1s spectra tracking EDTA decomposition. The scale bars are 10 nm.

preserves the ultrasmall architecture. However, when the temperature exceeds 600 °C, Ir particles begin sintering. By 800 °C, extensive coalescence produces particles with a broader size distribution (1–4 nm, with a mean of about 2 nm), representing more than twofold growth.

X-ray diffraction patterns (Fig. 4c) confirm that the TiN support maintains its crystalline structure across all annealing temperatures. The characteristic cubic TiN reflections at 36.7°, 42.6°, and 61.8° corresponding to (111), (200), and (220) planes show no shift or broadening. No TiO_2 peaks appear even after 800 °C treatment, demonstrating that the melamine/N_2 atmosphere prevents support oxidation. For Ir, no diffraction peaks appear in samples treated at ≤600 °C despite ~10 wt% loading, consistent with highly dispersed/sub-nanometer clusters below XRD detection. A weak Ir(111) reflection emerges only at 700 °C and becomes more pronounced at 800 °C, indicating coalescence into large particles, in agreement with TEM-observed sintering.

3.4.2 Surface chemical state. XPS analysis of Ir 4f core levels (Fig. 4d) reveals progressive reduction with increasing temperature. The as-synthesized sample exhibits predominantly oxidized Ir, with the Ir $4f_{7/2}$ peak at ~61.6 eV, characteristic of Ir^{4+} in IrO_2. This high oxidation state reflects strong coordination to oxygen and nitrogen donors from EDTA. At 400 °C, Ir remains largely oxidized, though a minor shoulder begins appearing near 60.9 eV, suggesting incipient reduction. At 500 °C, the Ir 4f spectrum shows a clear doublet structure: one component at 60.9 eV (metallic Ir^0) and another at 61.6 eV (Ir–O species).[22] This coexistence indicates a mixed Ir^0/Ir^{x+} state. As temperature increases to 600–800 °C, the metallic Ir^0 component progressively dominates, with the 800 °C sample showing almost exclusively the 60.8 eV peak characteristic of bulk metallic iridium.

XPS analysis of the N 1s region (Fig. 4e) tracks EDTA decomposition. The as-synthesized material shows a strong peak at 396.5 eV assigned to amine nitrogen coordinated to Ir^{3+} in the Ir–EDTA complex and a weak peak at 399.6 eV from N–C bonds in EDTA. At 400 °C, the peak at 399.6 eV shifts to ~398.9 eV and increases dramatically in intensity, indicating nitrogen dissociation from Ir centers and migration toward the TiN support as EDTA fragments. By 500 °C, the EDTA-derived nitrogen signal at 399.6 eV is essentially eliminated. At 700–800 °C, the spectrum is dominated by the Ti–N nitrogen peak at 396.4 eV, indistinguishable from the pristine support, confirming complete organic removal. Ti 2p XPS shows minimal changes across all temperatures, with peaks at ~463.4 eV and 457.7 eV remaining stable, indicating persistent Ti–N bonding. Together, these results confirm that the melamine-generated reducing atmosphere suppresses bulk TiN oxidation to insulating TiO_2 and preserves support conductivity.

3.4.3 Electronic properties. X-ray absorption near-edge structure (XANES) at the Ir L_3-edge (Fig. 5a) provides element-specific insight into Ir oxidation state evolution. The white-line feature intensity is proportional to unoccupied d-states. The as-synthesized and 400 °C samples exhibit high white-line intensity approaching the IrO_2 reference, indicating substantial Ir^{4+} character. As annealing temperature increases, white-line intensity systematically decreases, reflecting progressive reduction toward metallic Ir^0. Quantitative analysis (Fig. 5b) shows that white-line centroid energy shifts from 11 219.8 eV (as-synthesized, near IrO_2 at 11 220.0 eV) to 11 218.2 eV (800 °C, approaching Ir foil at 11 217.9 eV). The 500 °C sample occupies an intermediate position at 11 218.9 eV, confirming the presence of mixed Ir^0/Ir^{x+} species identified by XPS.

Extended X-ray absorption fine structure (EXAFS) analysis (Fig. 5c) reveals local coordination environment. The Fourier-transformed EXAFS spectra show two coordination shells: Ir–O/N at ~1.6 Å (phase-uncorrected) and Ir–Ir metallic bonds at ~2.7 Å. The as-synthesized material exhibits a dominant Ir–O peak with negligible Ir–Ir intensity, confirming isolated Ir atoms or very small clusters encapsulated by EDTA. At 400 °C, the Ir–O peak decreases while a small Ir–Ir peak emerges, indicating partial decomposition of the ligand shell and densification of Ir within still-confined, sub-nanometer clusters anchored at the original sites, rather than coalescence or the formation of bulk-like metallic bonding. By 500 °C, Ir–O and Ir–Ir intensities are comparable, reflecting small Ir^0 cores with mixture-coordinated surface species ($Ir–O/Ir^{x+}$) while the clusters remain sub-nm and spatially pinned. At 600–800 °C, the Ir–Ir peak becomes strongly dominant, and Ir–O nearly vanishes, indicating growth into bulk-like metallic nanoparticles.

Quantitative coordination number (CN) analysis from EXAFS fitting (Fig. 5d) shows a progressive transition with increasing temperature. The as-synthesized material shows CN(Ir–O) = 6.3 ± 0.8 and CN(Ir–Ir) = 0.2 ± 0.2, consistent with isolated Ir centers surrounded by EDTA. At 500 °C, CN(Ir–O) = 2.3 ± 0.3 and CN(Ir–Ir) = 5.3 ± 0.5, representing the crossover point. By

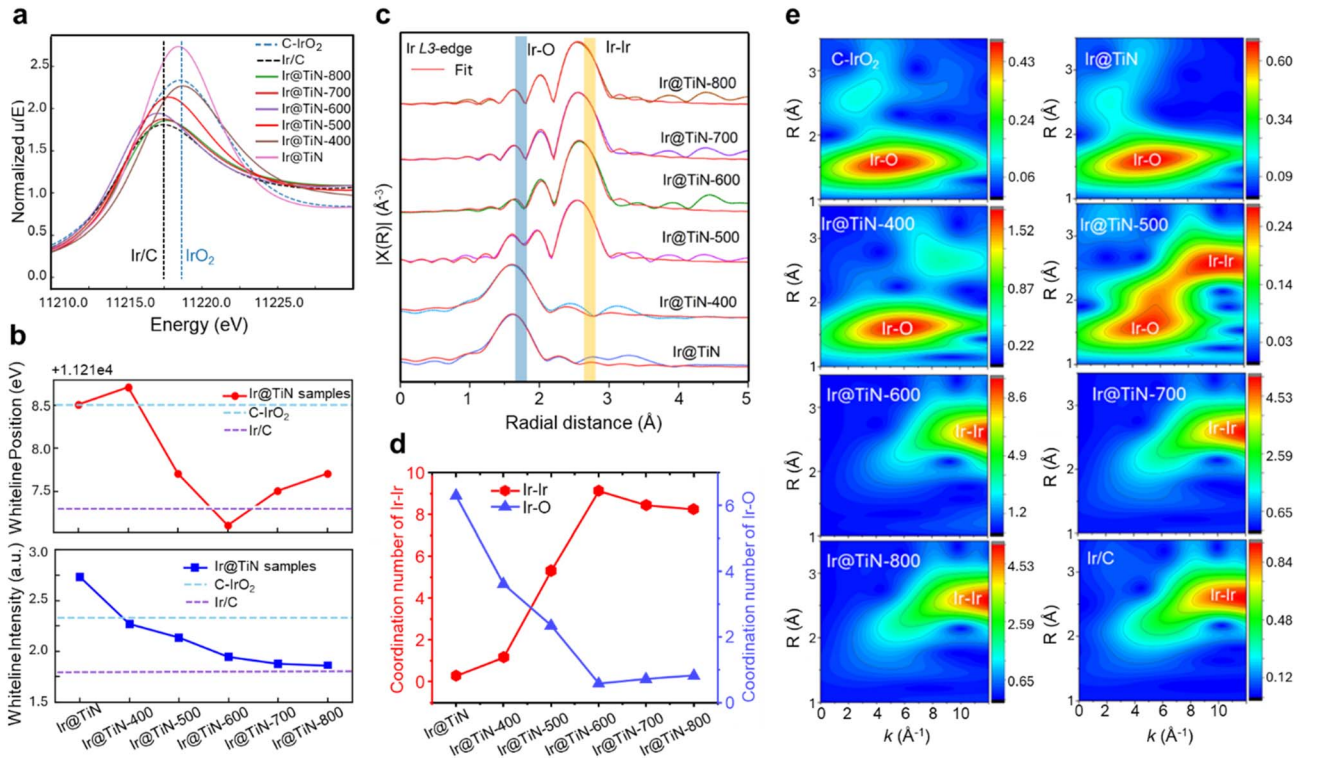

Fig. 5 XAS characterization of the thermal series. (a) XANES spectra showing progressive reduction with temperature. (b) White-line energy and intensity *versus* temperature. (c) Fourier-transformed EXAFS showing Ir–O (~1.6 Å) and Ir–Ir (~2.7 Å) coordination evolution. (d) Coordination numbers *versus* temperature: 500 °C shows CN(Ir–O) = 2.3 and CN(Ir–Ir) = 5.3. (e) Wavelet transform analysis for samples from as-synthesized to 800 °C.

800 °C, CN(Ir–O) drops to 0.8 ± 0.2, while CN(Ir–Ir) reaches 8.8 ± 1.1, approaching bulk metallic coordination (CN = 12 for fcc Ir). The Ir–Ir CN of 5.3 at 500 °C is consistent with a cuboctahedral 13-atom cluster (~0.75 nm diameter), which would have an average CN of ~5.5 for interior atoms. This agreement between EXAFS-derived coordination and TEM-measured size validates both techniques. In contrast, the 800 °C CN of 8.8 indicates particles approaching 2–4 nm with bulk-like coordination.

Wavelet transform (WT) analysis (Fig. 5e) provides enhanced *k*–*R* space resolution, separating light-atom (O, N) from heavy-atom (Ir) backscattering. The as-synthesized material (Fig. 5e) shows intensity concentrated at low *k*-values (2–6 $Å^{-1}$) and $R \sim 1.6$ Å, the signature of Ir–O/N coordination from EDTA. Ir@TiN-500 exhibits a bimodal pattern with intensity at both low *R*/distributed *k* (Ir–O contribution) and high *R*/high *k* ($R \sim 2.7$ Å, $k > 7$ $Å^{-1}$, Ir–Ir metallic scattering). This *k*–*R* fingerprint confirms the coexistence of two distinct coordination environments. Ir@TiN-800 shows predominantly high-*R*, high-*k* intensity, characteristic of extended Ir–Ir coordination in metallic Ir clusters.

The convergence of multiple characterization techniques establishes 500 °C as the optimal processing temperature. Below 500 °C, incomplete EDTA removal leaves organic barriers despite favorable particle size. Above 500 °C, complete organic elimination is achieved, but thermal energy triggers sintering. At 500 °C, three conditions coincide: (1) TEM and XRD confirm sub-nanometer size retention (0.75 nm) with crystallization, (2) XPS demonstrates complete EDTA removal, and (3) XAS reveals a mixed Ir^0/Ir^{x+} electronic state with both Ir–Ir and Ir–O coordinations. We interpret this mixed Ir^0/Ir^{x+} signature as an activity–stability trade-off: the coexistence of metallic domains (promoting conductivity) with surface oxide species (providing OER-active sites) enhances initial atomic utilization and kinetics, while under prolonged OER bias this mixed state can evolve irreversibly toward more oxygenated/disordered local structures, compromising long-term durability as revealed by *in situ* XAS in Section 3.6.

3.5 Electrochemical performance

We performed comparative studies of the electrochemical OER performance of all thermally treated samples to establish synthesis–structure–property relationships. Linear sweep voltammetry (LSV) in O_2-saturated 0.1 M $HClO_4$ reveals distinct performance differences across the thermal series (Fig. 6a). Ir@TiN-500 exhibits the highest OER activity, achieving 10 mA cm^{-2} (geometric current density) at an overpotential of 325 mV *vs.* RHE, substantially lower than that of commercial IrO_2 (390 mV). At 1.54 V, Ir@TiN-500 delivers a mass activity of 342 A g_{Ir}^{-1}, more than a fourfold improvement over commercial IrO_2 (76 A g_{Ir}^{-1}). Assuming (conservatively) that all Ir atoms in the catalyst are active, this mass activity corresponds to a minimum turnover frequency of ~0.17 s^{-1} per total Ir at 1.54 V (see the SI for calculation details). The as-synthesized and 400 °C samples show severely suppressed activity despite favorable particle size (~0.70 nm), suggesting that residual EDTA creates barriers for charge transfer. High-temperature samples (700–800 °C) exhibit moderate activity, superior to the ligand-blocked samples but inferior to 500 °C due to sintering-induced loss of surface area. Tafel analysis (Fig. 6b) provides insight into reaction kinetics. Ir@TiN-500 achieves a Tafel slope of 39.5 mV dec^{-1}, comparable to commercial IrO_2 (44.8 mV dec^{-1}) and indicating facile OER kinetics. In contrast, Ir@TiN-400 exhibits a Tafel slope of 182.8 mV dec^{-1}, reflecting sluggish charge transfer through residual EDTA barriers despite partial Ir reduction. The intermediate temperature samples (600–700 °C) show Tafel slopes of 50–65 mV dec^{-1}, while the 800 °C sample increases to ~70 mV dec^{-1}, consistent with reduced active site density from sintering.

Electrochemical surface area (ECSA) estimated from double-layer capacitance (C_{dl}) measurements (Fig. 6e) shows that Ir@TiN-500 exhibits the largest capacitance (6.16 mF cm^{-2}), confirming high accessibility of Ir surface atoms. This reflects the sub-nanometer particle size (0.9 nm) maintained after thermal treatment, where approximately 90% of atoms remain surface-exposed. Samples annealed at 700–800 °C show progressively lower C_{dl} (4.2 and 3.1 mF cm^{-2}, respectively) consistent with particle growth. The as-synthesized and 400 °C samples also exhibit low C_{dl} (2.8 and 3.4 mF cm^{-2}, respectively) despite favorable size, suggesting that residual EDTA physically blocks electrolyte access. ECSA-derived normalization is provided in Fig. S21b as a comparative metric, while noting that double-layer capacitance can be influenced by surface chemistry and wettability across ligand/annealing treatments. Ir@TiN-500 exhibits much higher ECSA-normalized activity than commercial IrO_2 after complete organic removal. At the same Ir loading, it also delivers the highest TOF, consistent with maximized site accessibility (Fig. S21a). Electrochemical impedance spectroscopy (EIS, Fig. 6d) quantifies interfacial charge-transfer resistance (R_{ct}). We note that EDTA pre-functionalization introduces an organic interlayer prior to annealing, which can transiently increase interfacial resistance in the as-prepared and low-temperature samples. After annealing, progressive ligand removal reduces this barrier and enables more direct electronic contact between Ir and TiN. Consistent with this interpretation, Ir@TiN-500 achieves the lowest R_{ct} of 19.2 Ω, indicating efficient charge transfer between Ir and TiN after EDTA removal, whereas the as-synthesized ($R_{ct} > 380$ Ω) and 400 °C ($R_{ct} > 4300$ Ω) samples exhibit high resistance, likely due to ligand-derived blocking and incomplete/heterogeneous interfacial cleaning (Table S1). At higher temperatures, R_{ct} increases again (51.7 Ω at 800 °C) despite complete organic removal and full Ir reduction to a metallic state, consistent with Ir coarsening that reduces the total Ir–TiN interfacial contact area per geometric electrode area. Notably, the fitted series resistance (R_s) varies only modestly across the thermal treatment using the same TiN support, whereas R_{ct} changes by orders of magnitude and tracks with ligand removal and interfacial contact evolution. This comparison confirms that the dominant differences arise from interfacial charge transfer rather than bulk support conductivity changes. Chronopotentiometric stability testing at 10 mA cm^{-2} shows that Ir@TiN-500 maintains stable potential for approximately 9.5

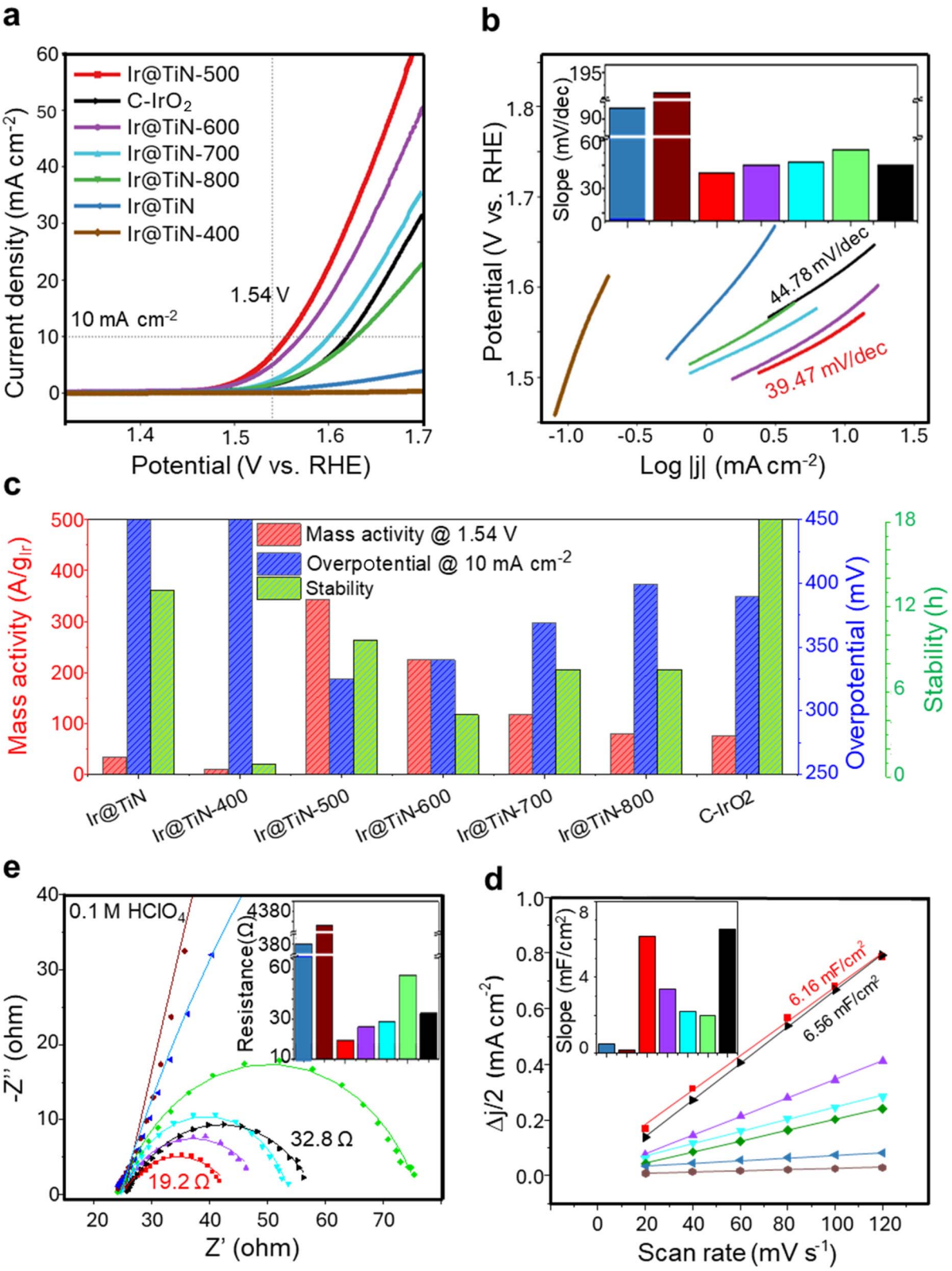

Fig. 6 Electrochemical OER performance of the thermal series. (a) LSV curves in 0.1 M $HClO_4$ (85% *iR*-corrected). (b) Tafel slopes. (c) Multimetric performance comparison: mass activity, overpotential, and stability. (d) EIS Nyquist plots showing charge-transfer resistance. (e) Double-layer capacitance indicating electrochemical surface area.

hours, the longest among the series, though still limited compared to state-of-the-art stable OER catalysts. This observation motivates the *in situ* XAS investigation (Section 3.6), which reveals that electronic/chemical transformation rather than sintering limits durability.

Fig. 6c summarizes the key performance metrics of catalysts treated at different temperatures. The volcano-shaped activity trend identifies 500 °C as optimal, with mass activity peaking sharply while overpotential reaches its minimum. This optimization reflects the balance between EDTA removal and size preservation: below 500 °C, EDTA blocks performance despite ideal size; above 500 °C, sintering reduces active site density despite clean interfaces. The correlation between structures featuring sub-nanometer size, mixed Ir^0/Ir^{x+}, and low R_{ct} and performance with high activity and large ECSA validates the advantage of the sequential synthesis design strategy. Representative literature benchmarks for acidic OER Ir-based catalysts (activity metrics, durability metrics, and test conditions) are summarized in Table S11; comparisons should be interpreted by taking into consideration differences in loading, electrolyte, *iR* correction, and metric definitions across reported literature. Within these constraints, the higher mass activity observed here is consistent with the high Ir utilization enabled by sub-nanometer Ir dispersion and efficient electronic contact with the conductive TiN support.

3.6 *In situ* X-ray absorption spectroscopy measurements

To understand the observed stability limitation, we first conducted post-stability TEM, which shows negligible particle agglomeration, indicating that sintering is not the primary degradation mechanism. To identify the electronic and chemical transformations occurring under OER conditions, we performed *in situ* XAS measurements at the Ir L_3-edge while applying controlled electrochemical potentials.

In situ XANES spectra for Ir@TiN-500 (Fig. 7a) show systematic evolution as potential increases from open-circuit (0.4 V) through the OER regime (1.32–1.65 V *vs.* RHE). The white-line intensity progressively increases and shifts to higher energy with applied potential, indicating oxidation of Ir ($Ir^0 \rightarrow Ir^{x+} \rightarrow Ir^{4+}$). The initial state at 0.4 V shows lower white-line intensity than commercial IrO_2, consistent with the mixed Ir^0/Ir^{x+} character established in Section 2.4. As the potential increases to 1.65 V, the white-line approaches but does not

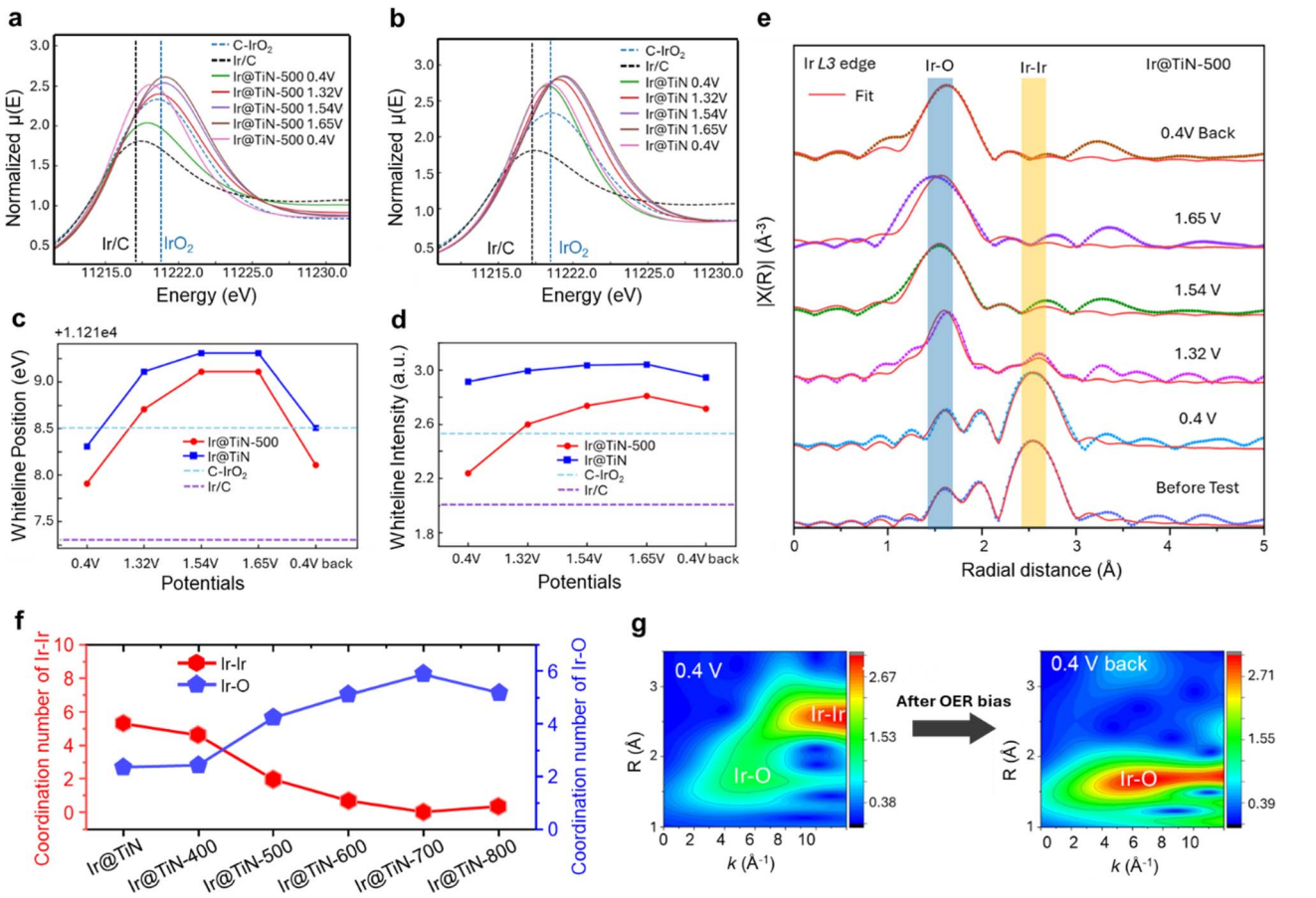

Fig. 7 *Operando* XAS during electrochemical cycling. (a and b) *Operando* XANES spectra during potential cycling (0.4 → 1.65 V → 0.4 V *vs.* RHE) of (a) Ir@TiN-500 and (b) Ir@TiN. (c) White-line energy evolution showing an ~0.4 eV residual shift. (d) White-line intensity showing ~30% irreversibility. (e) *Operando* Fourier-transformed EXAFS showing coordination changes. (f) Coordination number analysis showing permanent loss of Ir–Ir bonds and increase in Ir–O coordination. (g) Wavelet transform analysis for samples of Ir@TiN-500 at 0.4 V and back to 0.4 V.

reach the IrO_2 reference, suggesting partial surface oxidation rather than complete conversion to bulk oxide.

When potential is returned to 0.4 V after the OER scan, the white-line intensity does not fully recover to its initial state, revealing hysteresis indicative of irreversible oxidation. Quantitative analysis of the white-line position (Fig. 7c) shows that the centroid energy increases from 11 217.9 eV (initial 0.4 V) to 11 219.1 eV (1.65 V) and then decreases to only 11 218.1 eV upon return, leaving a residual shift of 0.3 eV. Similarly, integrated white-line intensity (Fig. 7c) increases from 2.0 to 2.6 a.u. during the forward scan but recovers to only 2.5 a.u. on the return. This persistent elevation indicates that a substantial fraction of Ir sites oxidized during the OER remain in higher oxidation states even after removing the driving potential. For comparison, *in situ* XANES of the as-synthesized Ir@TiN (Fig. 7b) shows different behavior. The initial white-line intensity is higher than that of Ir@TiN-500, reflecting the predominantly Ir^{4+} character from EDTA coordination. During the OER scan, the white-line changes less dramatically than Ir@TiN-500 and shows limited reversibility upon return. At all potentials, Ir@TiN-500 maintains lower white-line energy and intensity than the as-synthesized material before OER cycling, indicating more metallic character.

In situ Fourier-transformed EXAFS spectra (Fig. 7e) provide atomistic evidence for the oxidation process. At the initial 0.4 V state, Ir@TiN-500 shows the bimodal pattern established in Section 3.4: peaks at both ~1.9 Å (Ir–O) and ~2.7 Å (Ir–Ir). As potential increases to OER conditions, the Ir–O peak grows substantially while the Ir–Ir peak systematically weakens, consistent with oxidative conversion of metallic Ir–Ir bonds to Ir–O bonds. Upon returning to 0.4 V, the coordination environment shows limited recovery. The Ir–O peak remains elevated compared to the initial state, while the Ir–Ir peak fails to return to its original intensity. Quantitative coordination number analysis (Fig. 7f) shows that CN(Ir–Ir) decreases from 4.6 ± 0.5 (initial 0.4 V) to 0.7 ± 0.5 (1.54 V), representing a substantial loss of metallic bonds. Upon return to 0.4 V, CN(Ir–Ir) recovers to only 0.3 ± 0.9, indicating limited reversibility. Complementarily, CN(Ir–O) increases from 2.4 ± 0.3 (initial) to 5.9 ± 0.5 (1.65 V) and then decreases to 5.2 ± 1.2 upon return, remaining elevated above the initial value. These changes suggest substantial oxidative restructuring of the catalyst surface under OER conditions. Wavelet transform (WT) analysis shown in Fig. 7g also confirms the transformation of Ir–Ir to Ir–O during the OER process. The as-synthesized Ir@TiN shows different behavior under OER conditions (Fig. S18 and Table S10). Starting with predominantly Ir–O coordination (CN ~ 6.4, minimal Ir–Ir), it undergoes limited further changes during the potential cycle, consistent with already being in a stable oxidized state.

The *in situ* XAS results explain the ~9.5 hour OER stability limitation observed in Section 3.5. The irreversible oxidation revealed by XANES hysteresis and incomplete EXAFS coordination recovery indicates substantial restructuring of the ultrasmall Ir domains under OER conditions. Importantly, a decrease in the Ir–Ir EXAFS contribution can arise from multiple concurrent effects, including partial oxidation toward an IrO_x-like local structure, increased static/dynamic disorder, and fragmentation/restructuring that lowers the average metallic coordination number even if the total Ir loading remains similar. These trends are consistent with mechanistic understanding linking OER-driven restructuring (including lattice-oxygen processes) with Ir instability in acid;[23] however, Ir dissolution is not quantified in this work and cannot be concluded from *in situ* EXAFS alone. In addition, oxygen incorporation at the Ir–TiN interface may weaken metal–support interactions, as the formation of interfacial Ti–O–Ir bonding could disrupt the facile charge transfer established by thermal treatment. Overall, the mixed Ir^0/Ir^{x+} signature at 500 °C reflects an activity–stability trade-off: intimate contact with conductive TiN promotes high initial kinetics, while *in situ* XAS indicates irreversible oxidation/reconstruction toward more oxygenated/disordered motifs under acidic OER conditions, consistent with the observed stability limitation.

3.7 Structure–performance relationships

Fig. 8 provides an integrated view of how structural descriptors and OER performance interrelate across catalysts treated at different temperatures. The volcano plot (Fig. 8a) shows mass activity peaking at 500 °C while tracking particle size and Ir–O/Ir–Ir coordination numbers. The OER activity is suppressed when either EDTA persists (≤400 °C, high R_{ct} despite small size) or sintering occurs (≥700 °C, reduced surface area despite clean interfaces), with 500 °C representing the convergence of complete organic removal, sub-nanometer retention, and mixed Ir–O/Ir–Ir coordination.

Multi-parameter correlation analysis (Fig. 8b) demonstrates that mass activity correlates positively with C_{dl} ($R^2 = 0.82$) and CN(Ir–Ir) up to ~5 and inversely with R_{ct} ($R^2 = 0.89$) and particle size beyond 1 nm ($R^2 = 0.78$). These quantitative relationships confirm that the three requirements (sub-nanometer size, high coverage, and charge transfer between Ir and TiN) directly govern performance. The radar plot (Fig. 8c) integrating eight normalized metrics shows that Ir@TiN-500 exhibits a balanced profile across activity, kinetics, surface area, resistance, size, coordination, and stability. The correlation heatmap (Fig. 8d) confirms that activity strongly correlates with electronic ($1/R_{ct}$) and structural (C_{dl}, size) descriptors, while stability correlates weakly with initial performance metrics, indicating that degradation involves chemical/electronic transformation of Ir rather than structural coarsening.

4. Discussion

The sequential surface synthesis strategy addresses a persistent challenge in supported catalyst design: competing requirements that force trade-offs in conventional single-step methods. The key advance is recognizing that the multiple functions of EDTA, including surface anchoring, metal ion capture and growth confinement, become liabilities when operating simultaneously in one-pot synthesis, but are assets when exploited sequentially. By pre-installing surface templates before metal introduction, we reverse the thermodynamic preference from

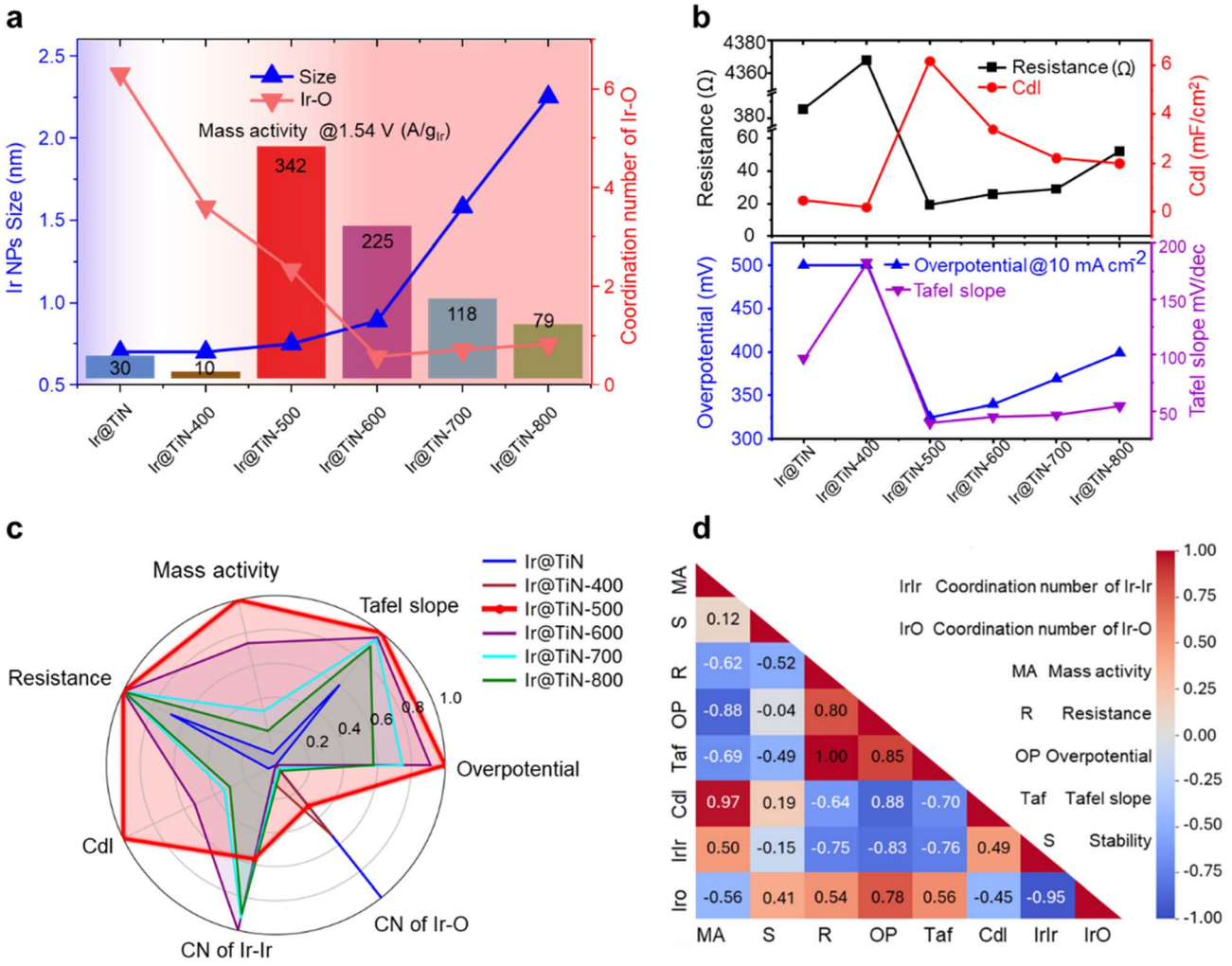

Fig. 8 Structure–performance relationships. (a) Volcano plot showing mass activity *versus* annealing temperature with overlaid particle size and coordination number trends. Background color indicates the Ir oxidation state (red: oxidized and blue: metallic). (b) Correlation plots of activity *versus* R_{ct}, Tafel slope, overpotential, and C_{dl}. (c) Radar plot comparing normalized performance metrics. (d) Correlation heatmap showing relationships among structural and performance descriptors.

solution-phase complexation to surface-directed coordination. This converts an unfavorable process into a favorable one, enabling independent optimization of coverage, size, and charge transfer. This principle may extend to other precious metal systems where ligand stabilization conflicts with surface attachment, provided that supports possess coordinating surface sites.

The integrated characterization reveals that activity maximization and stability represent distinct challenges requiring different strategies. The optimization of treatment temperature successfully balances organic removal with size preservation, creating a mixed Ir^0/Ir^{x+} coordination environment that combines high conductivity with OER activity. Quantitative structure–performance correlations establish clear design criteria for enhanced activity, which is enabled by sub-nanometer size, balanced metallic/oxidic character, and low interfacial resistance. However, *in situ* spectroscopic measurements reveal severe structural transformation: the high surface atom fraction that enables superior activity creates extreme vulnerability under harsh operating conditions. The mixed Ir^0/Ir^{x+} state undergoes oxidation during the OER, with loss of a large portion of metallic Ir–Ir bonds. This demonstrates that while sequential synthesis establishes stronger metal–support interactions than conventional methods, it cannot prevent fundamental structural transformation of the highly reactive sub-nanometer clusters. Future strategies to address this limitation could include: (1) controlled pre-oxidation to convert metallic Ir^0 to IrO_x species, establishing a more fully oxidized/oxygenated local structure. We note that while such oxidized structures are often associated with improved initial OER kinetics, they have also been linked in the literature to Ir instability pathways under acidic OER conditions, representing a complex optimization challenge. (2) Interface engineering to create stronger Ir–TiN bonding that prevents oxygen insertion at the interface, such as through controlled nitridation or introduction of interfacial buffer layers that maintain charge transfer

while blocking interfacial oxidation. The characterization framework combining *ex situ* multi-technique analysis with *in situ* measurements provides a methodology for evaluating these strategies and understanding degradation mechanisms in other supported catalyst systems. We note that translation from half-cell measurements to PEMWE-relevant current densities will additionally require catalyst-layer optimization, including higher Ir area loading and transport-engineered architectures to address mass transport limitations at high current densities. Such catalyst-layer engineering is beyond the scope of the present RDE-type evaluation but represents an important direction for future work toward practical device integration.

5. Conclusions

We demonstrate a four-step sequential surface-synthesis method that uniformly decorates TiN with a monolayer array of sub-nanometer Ir clusters in strong electronic contact with the support. EDTA acts as a temporary, multifunctional scaffold: first anchoring to TiN, then capturing Ir^{3+}, and finally confining growth, before removal. Optimal thermal treatment eliminates organic barriers while maintaining sub-nanometer Ir morphology, leading to enhanced OER mass activity. *In situ* XAS reveals that irreversible oxidation of Ir limits stability, highlighting that while sequential synthesis addresses the size-coverage-coupling challenge, stabilizing under-coordinated surface sites under harsh OER conditions requires future innovation. This work demonstrates that temporal decoupling of synthetic functions provides a general blueprint for synthesizing supported precious-metal catalysts.

Conflicts of interest

There are no conflicts to declare.

Data availability

The data supporting this article have been included as part of the supplementary information (SI). Additional relevant data and code are available from the corresponding authors upon request. Supplementary information: experimental details and data, Fig. S1–S21 and Tables S1–S11. See DOI: https://doi.org/10.1039/d5ta09528j.

Acknowledgements

This work was financially supported by the Division of Chemical Sciences, Geosciences, & Biosciences, Office of Basic Energy Sciences, Department of Energy, under contract DE-SC0012704 at Brookhaven National Laboratory (BNL FWP-CO-060). This research used resources of the Center for Functional Nanomaterials (CFN) and beamlines 7-BM (QAS), 11-BM (CMS) and 12-ID (SMI) of the National Synchrotron Light Source II (NSLS-II) U.S. DOE Office of Science User Facilities at Brookhaven National Laboratory under contract no. DE-SC0012704. Beamline operations were supported in part by the Synchrotron Catalysis Consortium (U.S. DOE, Office of Basic Energy Sciences, Grant No. DE-SC0012335). We thank Dr Xue Han for assistance with the XAS and OER data analysis.

References

1 L. An, C. Wei, M. Lu, H. Liu, Y. Chen, G. G. Scherer, A. C. Fisher, P. Xi, Z. J. Xu and C. H. Yan, *Adv. Mater.*, 2021, **33**, 2006328, DOI: 10.1002/adma.202006328.
2 H. Li, Y. Lin, J. Duan, Q. Wen, Y. Liu and T. Zhai, *Chem. Soc. Rev.*, 2024, **53**, 10709–10740, DOI: 10.1039/d3cs00010a.
3 G. Gao, Z. Sun, X. Chen, G. Zhu, B. Sun, S. Liu and Y. Yamauchi, *Appl. Catal., B: Environ. Energy*, 2023, **343**, 123584, DOI: 10.1016/j.apcatb.2023.123584.
4 Q. Shi, C. Zhu, D. Du and Y. Lin, *Chem. Soc. Rev.*, 2019, **48**, 3181–3192, DOI: 10.1039/c8cs00671g.
5 Y. Lin, Y. Dong, X. Wang and L. Chen, *Adv. Mater.*, 2022, **35**, 2210565, DOI: 10.1002/adma.202210565.
6 W. Zhao, F. Xu, L. Liu, M. Liu and B. Weng, *Adv. Mater.*, 2023, **35**(49), 2308060, DOI: 10.1002/adma.202308060.
7 Z. Jie, G. Yue, Z. Zhiqi, Z. Xilin, J. Qianqian, Z. Hua, S. Zhaoqi, L. Dongqing, Z. Jianrong, C. Chenghao, Z. Erhuan, W. Yuhao, H. Guangzhi, M. Muhammad Asim, R. Waseem, C. Xingke and C. Francesco, *Nat. Nanotechnol.*, 2024, **20**, 57–66, DOI: 10.1038/s41565-024-01807-x.
8 S. Liu, H. Tan, Y. C. Huang, Q. Zhang, H. Lin, L. Li, Z. Hu, W. H. Huang, C. W. Pao, J. F. Lee, Q. Kong, Q. Shao, Y. Xu and X. Huang, *Adv. Mater.*, 2023, **35**, 2305659, DOI: 10.1002/adma.202305659.
9 G. Meng, W. Sun, A. A. Mon, X. Wu, L. Xia, A. Han, Y. Wang, Z. Zhuang, J. Liu, D. Wang and Y. Li, *Adv. Mater.*, 2019, **31**, 1903616, DOI: 10.1002/adma.201903616.
10 H. Wei, J. Li, P. Du, L. Zhang, Z. Su, H. Li, M. Lei, X. Gong and K. Huang, *Adv. Compos. Hybrid Mater.*, 2023, **6**, 37, DOI: 10.1007/s42114-023-00625-4.
11 B. M. Tackett, W. C. Sheng and J. G. G. Chen, *Joule*, 2017, **1**, 253–263, DOI: 10.1016/j.joule.2017.07.002.
12 Z. P. Yu, J. Y. Xu, Y. F. Li, B. Wei, N. Zhang, Y. Li, O. Bondarchuk, H. W. Miao, A. Araujo, Z. C. Wang, J. L. Faria, Y. Y. Liu and L. F. Liu, *J. Mater. Chem. A*, 2020, **8**, 24743–24751, DOI: 10.1039/d0ta07093a.
13 H. Kim, J. Kim, J. Kim, G. H. Han, W. Guo, S. Hong, H. S. Park, H. W. Jang, S. Y. Kim and S. H. Ahn, *Appl. Catal., B*, 2021, **283**, 119596, DOI: 10.1016/j.apcatb.2020.119596.
14 C. Yang, W. Ling, Y. Zhu, Y. Yang, S. Dong, C. Wu, Z. Wang, S. Yang, J. Li, G. Wang, Y. Huang, B. Yang, Q. Cheng, Z. Liu and H. Yang, *Appl. Catal., B: Environ. Energy*, 2024, **358**, 124462, DOI: 10.1016/j.apcatb.2024.124462.
15 G. Zhao, P. Li, N. Cheng, S. X. Dou and W. Sun, *Adv. Mater.*, 2020, **32**, 2000872, DOI: 10.1002/adma.202000872.
16 E.-J. Kim, J. Shin, J. Bak, S. J. Lee, K. h. Kim, D. Song, J. Roh, Y. Lee, H. Kim, K.-S. Lee and E. Cho, *Appl. Catal., B*, 2021, **280**, 119433, DOI: 10.1016/j.apcatb.2020.119433.
17 H. Zhu, Y. Wang, Z. Jiang, B. Deng, Y. Xin and Z.-J. Jiang, *Adv. Energy Mater.*, 2024, **14**, 2303987, DOI: 10.1002/aenm.202303987.

18 S. Najafishirtari, C. Guglieri, S. Marras, A. Scarpellini, R. Brescia, M. Prato, G. Righi, A. Franchini, R. Magri, L. Manna and M. Colombo, *Appl. Catal., B*, 2018, **237**, 753–762, DOI: 10.1016/j.apcatb.2018.06.033.
19 T. W. van Deelen, C. Hernández Mejía and K. P. de Jong, *Nat. Catal.*, 2019, **2**, 955–970, DOI: 10.1038/s41929-019-0364-x.
20 H. Mou, J. J. Jeong, B. Lamichhane, S. Kattel, Z. C. Zhuang, J. H. Lee, Q. W. Chang and J. G. Chen, *Chem Catal.*, 2024, **4**(2), 100867, DOI: 10.1016/j.checat.2023.100867.
21 P. Lettenmeier, J. Majchel, L. Wang, V. A. Saveleva, S. Zafeiratos, E. R. Savinova, J. J. Gallet, F. Bournel, A. S. Gago and K. A. Friedrich, *Chem. Sci.*, 2018, **9**, 3570–3579, DOI: 10.1039/c8sc00555a.
22 X. Han, T. Mou, A. Islam, S. Kang, Q. Chang, Z. Xie, X. Zhao, K. Sasaki, J. A. Rodriguez, P. Liu and J. G. Chen, *J. Am. Chem. Soc.*, 2024, **146**, 16499–16510, DOI: 10.1021/jacs.4c02936.
23 O. Kasian, S. Geiger, T. Li, J. P. Grote, K. Schweinar, S. Y. Zhang, C. Scheu, D. Raabe, S. Cherevko, B. Gault and K. J. J. Mayrhofer, *Energy Environ. Sci.*, 2019, **12**, 3548–3555, DOI: 10.1039/c9ee01872g.